PHYSICAL REVIEW E **91**, 033108 (2015)

Fermionic path-integral Monte Carlo results for the uniform electron gas at finite temperature

V. S. Filinov,[1] V. E. Fortov,[1] M. Bonitz,[2] and Zh. Moldabekov[2]
[1]*Institute for High Temperatures, Russian Academy of Sciences, Izhorskaya 13, Bld. 1, Moscow 125412, Russia*
[2]*Institut für Theoretische Physik und Astrophysik, Christian-Albrechts-Universität zu Kiel, Leibnizstrasse 15, 24098 Kiel, Germany*

(Received 15 July 2014; revised manuscript received 17 January 2015; published 17 March 2015)

The uniform electron gas (UEG) at finite temperature has recently attracted substantial interest due to the experimental progress in the field of warm dense matter. To explain the experimental data, accurate theoretical models for high-density plasmas are needed that depend crucially on the quality of the thermodynamic properties of the quantum degenerate nonideal electrons and of the treatment of their interaction with the positive background. Recent fixed-node path-integral Monte Carlo (RPIMC) data are believed to be the most accurate for the UEG at finite temperature, but they become questionable at high degeneracy when the Brueckner parameter $r_s = a/a_B$—the ratio of the mean interparticle distance to the Bohr radius—approaches 1. The validity range of these simulations and their predictive capabilities for the UEG are presently unknown. This is due to the unknown quality of the used fixed nodes and of the finite-size scaling from $N = 33$ simulated particles (per spin projection) to the macroscopic limit. To analyze these questions, we present alternative direct fermionic path integral Monte Carlo (DPIMC) simulations that are independent from RPIMC. Our simulations take into account quantum effects not only in the electron system but also in their interaction with the uniform positive background. Also, we use substantially larger particle numbers (up to three times more) and perform an extrapolation to the macroscopic limit. We observe very good agreement with RPIMC, for the polarized electron gas, up to moderate densities around $r_s = 4$, and larger deviations for the unpolarized case, for low temperatures. For higher densities (high electron degeneracy), $r_s \lesssim 1.5$, both RPIMC and DPIMC are problematic due to the increased fermion sign problem.

DOI: 10.1103/PhysRevE.91.033108 PACS number(s): 52.65.−y, 05.30.Fk, 71.15.Nc, 05.70.Ce

I. INTRODUCTION

In recent years, interest in high-density plasmas has increased steadily. Examples are plasmas in the interior of the giant planets [1] and compact stars as well as highly compressed laboratory plasmas, such as laser plasmas or inertial confinement fusion plasmas [2]; for a recent experimental study, see [3]. In these systems, often the electrons are quantum degenerate and weakly (or moderately) coupled, whereas the ions are classical and moderately and sometimes strongly coupled. For both components it is crucial to include finite-temperature effects, which poses particular challenges for theory [4,5] and computer simulations; see, e.g., Refs. [6,7] and references therein.

The properties of the electron gas are a crucial ingredient to correctly describe dense plasmas as well as the electron gas in metals. Accurate data for the electron gas *at zero temperature* were provided long ago by quantum Monte Carlo simulations [8], and they have been widely used in density functional calculations. In the meantime, new and improved ground-state data have appeared, the most accurate ones, apparently, being the configuration interaction Monte Carlo data of Refs. [9,10]. However, these are all restricted to zero temperature and are not applicable to highly excited systems such as warm dense matter.

The extension of *ab initio* simulations to *finite temperature* is possible using the path integral Monte Carlo (PIMC) technique, e.g., [11–16], and many results have been obtained for fermions in the past two decades, including correlated electrons in quantum dots, e.g., [17,18], or dense plasmas, e.g., [19–23]. Only recently were PIMC simulations applied to the electron gas at finite temperature. Brown *et al.* presented restricted path-integral Monte Carlo (RPIMC) results that used the fixed node approximation [24] and cover a broad parameter range of the homogeneous electron gas. Subsequently, semianalytical fits were presented that intended to combine the RPIMC results with the known analytical limits [25]. A key problem of these data is that the accuracy of the results at high degeneracy is unknown since the fixed nodes used in the RPIMC simulations carry a systematic error that is difficult to quantify. The use of the ideal gas nodes appears to be problematic for the nonideal quantum Fermi gas (moderate r_s), where interaction effects may be relevant, as was shown for the case of hydrogen by Militzer *et al.* [19,26]. At the same time, these nodes are not able to reproduce the ideal Fermi gas limit ($r_s \to 0$), as was proven by one of us [27,28].

As a test, Brown *et al.* also performed fermionic simulations and observed increasing discrepancies at high degeneracy ($r_s \leqslant 1.5$). At the same time, they encountered large errors of their fermionic simulations since the average sign was very small, which is a direct manifestation of the fermion sign problem. A second important question is the extrapolation of the simulation data to the macroscopic limit. Note that the RPIMC simulations of Ref. [24] were done with just 33 particles per spin projection, and the authors subsequently employed a complex finite-size-scaling procedure. We note that this issue is still unresolved, and subsequent works applied very different finite-size scalings to the RPIMC data [25,29,30]. Thus, the question of reliable high-temperature data for the uniform electron gas at high densities remains.

Therefore, the motivation of the present work is to perform independent first-principles direct fermionic PIMC simulations and compare them to the earlier results. Toward that end, we make use of a PIMC approach that was developed several years ago and successfully applied to dense hydrogen [31–33], hydrogen-helium mixtures [34,35], electron-hole plasmas in semiconductors [36,37] and nonideal quark-gluon plasma [38,39]. To simulate the uniform electron gas, the code is modified such that the positive charge component is treated as a quantum gas neglecting correlations. Furthermore, to be able to simulate situations of high degeneracy, the treatment of exchange effects is substantially improved. Finally, to reduce the issue of finite-size effects, we use significantly larger particle numbers than previous simulations. We avoid artificial finite-size corrections and, instead, use a modified treatment of periodic boundary conditions proposed by Yakub *et al.* [40], together with an extrapolation with respect to the particle number. Details of the PIMC scheme are described in Sec. II.

Our numerical results are presented in Sec. III. There we demonstrate the improved treatment of fermionic exchange via a comparison with the analytical data for the ideal Fermi gas. Our comparison with the RPIMC data reveals very good agreement for low and moderate densities, $r_s \gtrsim 4$, for the polarized electron gas, and slightly larger deviations for the unpolarized case at temperatures below the Fermi temperature.

II. FERMIONIC PATH-INTEGRAL MONTE CARLO SIMULATIONS

A. Jellium model

The neutral uniform electron gas (UEG) or jellium is a quantum-mechanical model of interacting electrons where the positive charges (e.g., atomic nuclei of a solid) are assumed to form a uniform background that assures overall charge neutrality but which is not treated microscopically. The model allows one to focus on the effects that occur due to the quantum nature of electrons and their repulsive interactions, and to treat the electron-electron interaction rigorously. The artificial and structureless background charge interacts electrostatically with itself and the electrons.

The jellium Hamiltonian (for a textbook discussion, see Ref. [41]) for N electrons confined within a volume V having the microscopic density $\rho(r) = \sum_{a=1}^{N} \delta(r - r_a)$ and background charge density $n(R) = N/V$ is

$$\hat{H} = \hat{H}_{\text{el}} + \hat{H}_{\text{back}} + \hat{H}_{\text{el-back}}, \tag{1}$$

where $\hat{H}_{\text{el}}$ is the electron Hamiltonian consisting of kinetic and electron-electron repulsion terms:

$$\hat{H}_{\text{el}} = \sum_{a=1}^{N} \frac{\hat{p}_a^2}{2m} + \sum_{a<b}^{N} \frac{e^2}{|\hat{r}_a - \hat{r}_b|}. \tag{2}$$

$\hat{H}_{\text{back}}$ is the Hamiltonian of the positive background charge describing its electrostatic self-interaction. Its expectation value is

$$\begin{aligned}\langle \hat{H}_{\text{back}} \rangle &= \frac{e^2}{2} \int_V dR \int_V dR' \frac{n(R)n(R')}{|R - R'|} \\ &= \frac{e^2}{2} \frac{N^2}{V^2} \int_V dR \int_V dR' \frac{1}{|R - R'|} = \frac{N^2}{2V} \lim_{\mathbf{q}\to 0} v_q,\end{aligned} \tag{3}$$

where we introduced the Fourier component of the Coulomb potential, $v_q = \frac{4\pi e^2}{q^2}$. The contribution of the electrostatic electron-background interaction is given by

$$\begin{aligned}\langle \hat{H}_{\text{el-back}} \rangle &= -\int_V dr \int_V dR \frac{e^2 \rho(r) n(R)}{|r - R|} \\ &= -e^2 \frac{N}{V} \sum_{a=1}^{N} \int_V dR \frac{1}{|r_a - R|} = -\frac{N^2}{V} \lim_{\mathbf{q}\to 0} v_q.\end{aligned} \tag{4}$$

In a finite system, the results (3) and (4) are finite because q approaches a finite minimal value determined by the system volume. If, however, the thermodynamic limit is taken, this limit for q becomes zero, as indicated in the formulas, and the two results diverge. This divergence is exactly canceled by the $q = 0$ contribution of the electron-electron interaction, which has the form [41]

$$\frac{N(N-1)}{2V} \lim_{\mathbf{q}\to 0} v_q. \tag{5}$$

This cancellation is due to the assumption of charge neutrality and allows one to neglect the background contribution entirely and just study the electron component, omitting the $q = 0$ contribution (i.e., the spatially homogeneous part) to the thermodynamic quantities.

In our simulations, we employ a finite simulation cell. For this case, again, the background related energies can be calculated. Assuming, for simplicity, a spherical simulation cell of radius R with a particle number chosen such that a given density n is realized, i.e., $N = n\frac{4\pi}{3}R^3$, one readily obtains from standard electrostatics for the background energy (electrostatic self-energy)

$$\langle \hat{H}_{\text{back}} \rangle(N) = \frac{3}{5} \frac{Q^2}{R(N)}. \tag{6}$$

Similarly, the interaction energy of N electrons homogeneously distributed in this sphere with the homogeneous charge background is found to be

$$\langle \hat{H}_{\text{el-back}} \rangle(N) = -\frac{6}{5} \frac{Q^2}{R(N)} \equiv -2\langle \hat{H}_{\text{back}} \rangle(N), \tag{7}$$

and it equals exactly minus two times the background energy, independently of the system size. Both terms diverge with increasing system size. But one readily sees that the sum of both energies, again, is exactly canceled by the analogous contribution of the electrons, which equals $\langle \hat{H}_{\text{back}} \rangle(N)$. This underlines that all electrostatic mean-field contributions compensate each other, and the nonvanishing reminder of the interaction energy is just due to electronic correlations, i.e., density fluctuations around the uniform density.

We can now estimate the scaling of the background energy contribution with system size and density. Toward that end, we switch to atomic units introducing the density (Brückner) parameter, $r_s = a/a_B$, where the mean interparticle distance is given by $a = [\frac{3}{4\pi n}]^{1/3}$, a_B denotes the Bohr radius, and energies are given in Hartrees, with $1\ \text{Ha} = \frac{e^2}{4\pi\epsilon_0}\frac{1}{a_B}$. Then we obtain for the background energy per particle:

$$\frac{\langle \hat{H}_{\text{back}} \rangle(N)}{N\ \text{Ha}} = \frac{3}{5} \frac{N^{2/3}}{r_s}. \tag{8}$$

B. Path-integral representation of thermodynamic quantities

Particle simulations of Coulomb systems face the problem of an unlimited increase of the interaction energy at small distances. Quantum simulations such as path-integral Monte Carlo avoid the Coulomb divergences in a natural way. This has been demonstrated before for PIMC simulations of two-component electron-ion plasmas, e.g., [32,33], and electron-hole plasmas [37]. Here we adapt these simulations to jellium by treating it as the limiting case of the neutral two-component plasma ($N_e = N_p = N$), where, in the end, the background component (the ions) will be treated as noninteracting.

Let us start from a quantum two-component Coulomb system of electrons and positive charges in equilibrium with the Hamiltonian, $\hat{H} = \hat{K} + \hat{U}^c$, containing kinetic energy $\hat{K}$ and Coulomb interaction energy contributions, $\hat{U}^c = \hat{U}^c_{pp} + \hat{U}^c_{ee} + \hat{U}^c_{ep}$. The thermodynamic properties in the canonical ensemble with given temperature T and fixed volume V are fully described by the density operator $\hat{\rho} = e^{-\beta\hat{H}}$, with the partition function

$$Z(N_e,N_p,V;\beta) = \frac{1}{N_e!N_p!}\sum_{\sigma}\int_V dq\,\rho(q,\sigma;\beta), \qquad (9)$$

where $\beta = 1/k_BT$, and $\rho(q,\sigma;\beta)$ denotes the diagonal elements of the density matrix in coordinate representation at a given value σ of the total spin. In Eq. (9), $q = \{q_e,q_p\}$ and $\sigma = \{\sigma_e\}$ are the spatial coordinates of electrons and protons and spin degrees of freedom of the electrons, i.e., $q_a = \{q_{1,a}\cdots q_{l,a}\cdots q_{N_a,a}\}$ and $\sigma_e = \{\sigma_{1,e}\cdots\sigma_{l,e}\cdots\sigma_{N_e,e}\}$. To calculate thermodynamic functions, the logarithm of the partition function has to be differentiated with respect to thermodynamic variables. For example, for pressure and internal energy, it follows that

$$\beta p = \frac{\partial \ln Z}{\partial V} = \left[\frac{\alpha}{3V}\frac{\partial \ln Z}{\partial \alpha}\right]_{\alpha=1}, \qquad (10)$$

$$\beta E = -\beta\frac{\partial \ln Z}{\partial \beta}, \qquad (11)$$

where $\alpha = L/L_0$ is a length scaling parameter.

The exact density matrix of interacting quantum systems is not known (particularly for low temperatures and high densities), but it can be constructed using a path-integral approach [11] based on the operator identity,

$$e^{-\beta\hat{H}} = e^{-\Delta\beta\hat{H}}e^{-\Delta\beta\hat{H}}\cdots e^{-\Delta\beta\hat{H}}, \quad \Delta\beta = \beta/(n+1), \qquad (12)$$

which involves $n+1$ identical high-temperature factors with temperature $(n+1)T$, which allows us to rewrite the integral in Eq. (9),

$$\begin{aligned}&\sum_{\sigma}\int dq^{(0)}\,\rho(q^{(0)},\sigma;\beta)\\ &\quad= \int dq^{(0)}\cdots dq^{(n)}\,\rho^{(1)}\rho^{(2)}\,\cdots\rho^{(n)}\\ &\quad\quad\times\sum_{\sigma}\sum_{P_e}(\pm 1)^{\kappa_{P_e}}\,\mathcal{S}(\sigma,\hat{P}_e\sigma'_a)\,\hat{P}_e\rho^{(n+1)}\Big|_{q^{(n+1)}=q^{(0)},\sigma'=\sigma}.\end{aligned} \qquad (13)$$

The spin gives rise to the spin part of the density matrix ($\mathcal{S}$) with exchange effects accounted for by the permutation operator $\hat{P}_e$ acting on the electron coordinates $q^{(n+1)}$ and spin projections σ'. The sum is over all permutations with parity κ_{P_e}. Equation (13) involves the off-diagonal high-temperature density matrices, $\rho^{(l)} \equiv \rho\left(q^{(l-1)},q^{(l)};\Delta\beta\right) = \langle q^{(l-1)}|e^{-\Delta\beta\hat{H}}|q^{(l)}\rangle$, where $l = 1,\ldots,n+1$. Accordingly, each particle is represented by a set of $n+1$ coordinates ("beads"), i.e., the whole configuration of the particles is represented by a $3(N_e+N_p)(n+1)$-dimensional vector

$$\begin{aligned}\tilde{q} \equiv \{&q^{(0)}_{1,e},\ldots,q^{(n+1)}_{1,e},q^{(0)}_{2,e},\ldots,q^{(n+1)}_{2,e},\\ &\ldots,q^{(n+1)}_{N_e,e};q^{(0)}_{1,p},\ldots,q^{(n+1)}_{N_p,p}\}.\end{aligned} \qquad (14)$$

To determine the energy in the path-integral representation (13), each high-temperature density matrix has to be differentiated [15,33],

$$\begin{aligned}\beta E = &-\frac{1}{Z}\int dq^{(0)}\cdots dq^{(n)}\sum_{\sigma}\sum_{P_e}(\pm 1)^{\kappa_{P_e}}\,\mathcal{S}(\sigma,\hat{P}_e\sigma')\\ &\times\sum_{k=1}^{n+1}\rho^{(1)}\cdots\rho^{(l-1)}\left[\beta\frac{\partial\rho^{(l)}}{\partial\beta}\right]\rho^{(l+1)}\\ &\cdots\rho^{(n)}\hat{P}_e\rho^{(n+1)}\Big|_{q^{(n+1)}=q^{(0)},\,\sigma'=\sigma}.\end{aligned} \qquad (15)$$

It is straightforward to show that the matrix elements $\rho^{(l)}$ can be rewritten as

$$\begin{aligned}\rho^{(l)} &\equiv \langle q^{(l-1)}|e^{-\Delta\beta\hat{H}}|q^{(l)}\rangle\\ &= \int d\tilde{p}^{(l-1)}d\bar{p}^{(l)}\,\langle q^{(l-1)}|e^{-\Delta\beta\hat{U}^c}|\tilde{p}^{(l-1)}\rangle\\ &\quad\times\langle\tilde{p}^{(l-1)}|e^{-\Delta\beta\hat{K}}\,|\bar{p}^{(l)}\rangle\langle\bar{p}^{(l)}|e^{-\frac{\Delta\beta^2}{2}[\hat{K},\hat{U}^c]}\cdots|q^{(l)}\rangle,\end{aligned} \qquad (16)$$

where $\tilde{p}^{(l-1)}(\bar{p}^{(l)})$ are the conjugate variables to $q^{(l-1)}(q^{(l)})$. To further evaluate the derivatives in Eq. (15), it is convenient to introduce dimensionless integration variables $\eta^{(l)} = (\eta^{(l)}_p,\eta^{(l)}_e)$, where $\eta^{(l)}_a = \kappa_a(q^{(l)}_a - q^{(l-1)}_a)$ for $l = 1,\ldots,n$, and we introduced the dimensional factor $\kappa^2_a \equiv m_a/(2\pi\hbar^2\Delta\beta) = 1/\lambda^2_{\Delta,a}$ for $a = e,p$. The main advantage is that differentiation of the density matrix now affects only the interaction terms,

$$\beta\frac{\partial\rho^{(l)}}{\partial\beta} = -\beta\frac{\partial[\Delta\beta U^c(X^{(l-1)})]}{\partial\beta}\rho^{(l)} + \beta\tilde{\rho}^{(l)}_{\beta}, \qquad (17)$$

where

$$\begin{aligned}\tilde{\rho}^{(l)}_{\beta} = &\int dp^{(l)}\,\langle X^{(l-1)}|e^{-\Delta\beta\hat{U}^c}|p^{(l)}\rangle e^{-\frac{\langle p^{(l)}|p^{(l)}\rangle}{4\pi(n+1)}}\\ &\times\langle p^{(l)}|\frac{\partial}{\partial\beta}e^{-\frac{(\Delta\beta)^2}{2}[\hat{K},\hat{U}^c]}\,\cdots|X^{(l)}\rangle,\end{aligned} \qquad (18)$$

with $p^{(l)}_a = \tilde{p}^{(l)}_a/(\kappa_a\hbar)$, $p(l) \equiv (p^{(l)}_p,p^{(l)}_e)$, in accordance with Eq. (16). Furthermore, $X^{(0)} \equiv (\kappa_p q^{(0)}_p,\kappa_e q^{(0)}_e)$, $X^{(l)} \equiv (X^{(l)}_p,X^{(l)}_e)$ with $X^{(l)}_a = \kappa_a q^{(0)}_a + \sum_{l=1}^{k}\eta^{(l)}_a$ (k runs from 1 to n), and $X^{(n+1)} \equiv (\kappa_p q^{(n+1)}_p,\kappa_e q^{(n+1)}_e) = X^{(0)}$.

For $k = n + 1$, we have

$$\beta \frac{\partial}{\partial \beta}\, \hat{P}_e \rho^{(n+1)} = -\beta \frac{\partial \Delta\beta U^c(X^{(n)})}{\partial \beta} \hat{P}_e \rho^{(n+1)} + \beta \hat{P}_e \tilde{\rho}_\beta^{(n+1)}\,, \tag{19}$$

and, together with Eq. (15), we obtain for the energy

$$\beta E = \frac{3}{2}(N_e + N_p) - \frac{1}{Z}\frac{1}{\lambda_p^{3N_h}\lambda_e^{3N_e}} \int_V dq^{(0)} d\eta^{(1)} \cdots d\eta^{(n)} \sum_\sigma \sum_{P_e} (\pm 1)^{\kappa_{P_e}}\, \mathcal{S}(\sigma, \hat{P}_e \sigma')$$
$$\times \left\{ \sum_{k=1}^{n+1} \rho^{(1)} \cdots \rho^{(l-1)} \left[\beta \tilde{\rho}_\beta^{(l)} - \beta \frac{\partial \Delta\beta U^c(X^{(l-1)})}{\partial \beta} \rho^{(l)} \right] \rho^{(l+1)} \cdots\, \rho^{(n)} \hat{P}_e \rho^{(n+1)} \right\} \Bigg|_{X^{(n+1)} = X^{(0)},\, \sigma' = \sigma} . \tag{20}$$

This way, the derivatives of the density matrix have been calculated and we turn to the next point: finding approximations for the high-temperature density matrices $\rho^{(l)}$.

C. High-temperature asymptotics of the density matrix: The Kelbg potential

In this section, we discuss approximations for the high-temperature density matrix that can be used for efficient direct PIMC simulations. Our approach involves effective quantum pair potentials Φ_{ab}, which are approximated by the Kelbg potential. Here, we closely follow our earlier work [33], in which details and further references can be found.

1. *Pair approximation and the Kelbg potential*

The N-particle high-temperature density matrix is expressed in terms of two-particle density matrices (higher-order terms become negligible at sufficiently high temperature, i.e., for a large number n of imaginary "time slices") given by

$$\rho_{ab}(q_{k,a}, q'_{k,a}, q_{t,b}, q'_{t,b}; \beta)$$
$$= \frac{(m_a m_b)^{3/2}}{(2\pi\hbar\beta)^3} \exp\left[-\frac{m_a}{2\hbar^2\beta}(q_{k,a} - q'_{k,a})^2 \right]$$
$$\times \exp\left[-\frac{m_b}{2\hbar^2\beta}(q_{t,b} - q'_{t,b})^2 \right] \exp\left[-\beta \Phi_{ab}^{\mathrm{OD}} \right], \tag{21}$$

where $a,b = e,p$ and $k,t = 1,\ldots,N$. This result is obtained from factorization into kinetic and interaction parts, $\rho_{ab} \approx \rho_0^K \rho_{ab}^{U^c}$, which is exact in the classical case, i.e., at sufficiently high temperature. The error made at finite temperature vanishes with the number of time slices as n^{-2}; cf. Ref. [33]. The off-diagonal density matrix element (21) involves an effective pair interaction that is approximated by its diagonal elements according to $\Phi_{ab}^{\mathrm{OD}}(q_{k,a}, q'_{k,a}, q_{t,b}, q'_{t,b}; \beta) \approx \frac{1}{2}[\Phi_{ab}(q_{k,a} - q_{t,b}; \beta) + \Phi_{ab}(q'_{k,a} - q'_{t,b}; \beta)]$, for which we use the familiar Kelbg potential [42,43],

$$\Phi_{ab}(x_{ab}; \beta) = \frac{e_a e_b}{\lambda_{ab} x_{ab}} [1 - e^{-x_{ab}^2} + \sqrt{\pi}\, x_{ab} \{1 - \mathrm{erf}(x_{ab})\}], \tag{22}$$

where $x_{ab} = |q_{k,a} - q_{t,b}|/\lambda_{ab}$, and we introduced the error function, $\mathrm{erf}(x) = \frac{2}{\sqrt{\pi}} \int_0^x dt\, e^{-t^2}$. Note that the Kelbg potential is finite at zero distance, which is a consequence of quantum effects. The validity of this potential as well as of the diagonal approximation is restricted to temperatures substantially higher than the binding energy [44–46], which puts another lower bound on the number of time slices n. For completeness, we also note other effective potentials, e.g., Refs. [47,48], as well as recently derived improved versions that are applicable to strong coupling [45,46].

Summarizing, we can conclude that, with the approximations (21) and (22), each of the high-temperature density matrix factors on the right-hand side of Eq. (13) carries an error of the order $1/(n+1)^2$,

$$\rho^{(l)} = \rho_0^{(l)} e^{-\Delta\beta U(X^{(l-1)})} \delta(X^{(l-1)} - X^{(l)}) + O[(n+1)^{-2}], \tag{23}$$

where $\rho_0^{(l)}$ is the kinetic density matrix, and U denotes the sum of all interaction energies, each consisting of the respective sum of pair interactions given by Kelbg potentials, $U(X^{(l)}) = U_{pp}(X_p^{(l)}) + U_{ee}(X_e^{(l)}) + U_{ep}(X_p^{(l)}, X_e^{(l)})$.

2. *Estimator for the total energy*

Let us now return to the computation of thermodynamic functions and derive the final expressions, following from Eq. (23), that will be used in the simulations. First, we note that in Eq. (20), special care has to be taken in performing the derivatives of the Coulomb potentials with respect to β: Products $\beta \frac{\partial \Delta\beta \cdot U^c(X^{(l-1)})}{\partial \beta}$ have a singularity at zero interparticle distance that is integrable but leads to difficulties in the simulations. To assure efficient simulations, we transform the e-e, p-p, and e-p contributions in the following way:

$$\langle X^{(l-1)} | e^{-\Delta\beta \hat{K}} | X^{(l)} \rangle \left[-\beta \frac{\partial}{\partial \beta} [\Delta\beta U^c(X^{(l-1)})] \right]$$
$$\approx \int_0^1 d\alpha \int d\tilde{X}^{(l-1)} \langle X^{(l-1)} | e^{-\Delta\beta\alpha \hat{K}} | \tilde{X}^{(l-1)} \rangle$$
$$\times \left[-\beta \frac{\partial}{\partial \beta} (\Delta\beta U^c(\tilde{X}^{(l-1)})) \right]$$
$$\times \langle \tilde{X}^{(l-1)} | e^{-\Delta\beta(1-\alpha)\hat{K}} | X^k \rangle + O[(n+1)^{-2}]$$
$$\approx \langle X^{(l-1)} | e^{-\Delta\beta \hat{K}} | X^{(l)} \rangle \left[-\beta \frac{\partial}{\partial \beta} [\Delta\beta U(X^{(l-1)})] \right]$$
$$+ O[(n+1)^{-2}], \tag{24}$$

where $\langle \cdots | \cdots \rangle$ denotes the scalar product. This means that within the standard error of our approximation, $O(n^{-2})$, we have replaced the sum of the Coulomb potentials U^c by the corresponding sum of Kelbg potentials U, which is much better suited for MC simulations. This result coincides with expressions that can be obtained if we first choose an approximation for the high-temperature density matrices $\rho^{(l)}$ using the Kelbg potential and then take the derivatives.

Thus, our final result for the energy is

$$\beta E = \frac{3}{2}(N_e + N_p) + \frac{1}{Z}\frac{1}{\lambda_p^{3N_p}\lambda_e^{3N_e}}\sum_{s=0}^{N_e}\int_V dq^{(0)}d\eta^{(1)}\cdots d\eta^{(n)}\,\rho_s(q^{(0)},\eta^{(1)},\ldots,\eta^{(n)},\beta)$$
$$\times\Bigg\{\sum_{l=0}^{n}\Bigg[\sum_{k=1}^{N_p}\sum_{t=1}^{N_e}\Phi_{ep}(|x_{kt}^l|) + \sum_{k<t}^{N_p}\Phi_{ee}(|r_{kt}^l|) + \sum_{k<t}^{N_e}\Phi_{pp}(|q_{kt}^l|)\Bigg]$$
$$+\sum_{l=1}^{n}\Bigg[\sum_{k=1}^{N_p}\sum_{t=1}^{N_e}D(x_{kt}^l)\frac{\partial\Delta\beta\Phi_{ep}}{\partial|x_{kt}^l|} + \sum_{k<t}^{N_e}C(r_{kt}^l)\frac{\partial\Delta\beta\Phi_{ee}}{\partial|r_{kt}^l|} + \sum_{k<t}^{N_e}C(q_{kt}^l)\frac{\partial\Delta\beta\Phi_{pp}}{\partial|q_{kt}^l|}\Bigg] - \frac{1}{\det||\psi_{kt}^{n,0}||_s}\frac{\partial\det||\psi_{kt}^{n,0}||_s}{\partial\beta}\Bigg\}, \quad (25)$$

with the definitions

$$C(r_{kt}^l) = \frac{\langle r_{kt}^l|y_{kt}^l\rangle}{2|r_{kt}^l|}, \qquad C(q_{kt}^l) = \frac{\langle q_{kt}^l|\tilde{y}_{kt}^l\rangle}{2|q_{kt}^l|},$$
$$D(x_{kt}^l) = \frac{\langle x_{kt}^l|y_p^l - \tilde{y}_t^l\rangle}{2|x_{kt}^l|}, \quad \Psi_{ab}(x) \equiv \Delta\beta\frac{\partial[\beta'\Phi_{ab}(x,\beta')]}{\partial\beta'|_{\beta'=\Delta\beta}}.$$

Here we introduced the following notation for the differences of two coordinate vectors:

$$q_{kt} \equiv q_{k,p} - q_{t,p}, \qquad r_{kt} \equiv q_{k,e} - q_{t,e}, \qquad x_{kt} \equiv q_{k,e} - q_{t,p},$$
$$r_{kt}^l = r_{kt} + y_{kt}^l, \qquad q_{kt}^l = q_{kt} + \tilde{y}_{kt}^l, \qquad x_{kt}^l \equiv x_{kt} + y_k^l - \tilde{y}_t^l,$$
$$y_{kt}^l \equiv y_k^l - y_t^l, \qquad \tilde{y}_{kt}^l \equiv \tilde{y}_p^l - \tilde{y}_t^l,$$

with $y_t^l = \Delta\lambda_e\sum_{k'=1}^{l}\eta_t^{(k')}$ and $\tilde{y}_k^l = \Delta\lambda_p\sum_{k'=1}^{l}\tilde{\eta}_k^{(k')}$. The density matrices ρ_s appearing in Eq. (25) are given by

$$\rho_s = C_{N_e}^s\, e^{-\beta U}\det||\psi_{kt}^{n,0}||_s\prod_{l=1}^{n}\prod_{k=1}^{N_e}\prod_{t=1}^{N_p}\phi_k^l\,\tilde{\phi}_t^l, \qquad (26)$$

where U is the total interaction energy comprised of contributions from all time slices,

$$U = \frac{1}{n+1}\sum_{l=0}^{n}\{U_e(X_e^{(l)},\Delta\beta) + U_p(X_p^{(l)},\Delta\beta)$$
$$+ U_{ep}(X_p^{(l)},X_e^{(l)},\Delta\beta)\}, \qquad (27)$$

and we defined

$$\phi_t^l \equiv \exp[-\pi|\eta_t^{(l)}|^2], \qquad \tilde{\phi}_k^l \equiv \exp[-\pi|\tilde{\eta}_k^{(l)}|^2], \qquad (28)$$
$$||\psi_{kt}^{n,0}||_s = \|e^{-\frac{\pi}{\Delta\lambda_e^2}|(r_k-r_t)+y_k^n|^2}\|_s\,\|e^{-\frac{\pi}{\Delta\lambda_e^2}|(r_k-r_t)+y_k^n|^2}\|_{N_e-s}.$$

Notice that the density matrix (26) does not contain an explicit sum over the permutations, and thus no sum of terms with alternating sign. Instead, the whole exchange problem is contained in the determinant (28), which is a product of exchange matrices of electrons, where s denotes the number of electrons having the same spin projections (for more details, we refer to Ref. [49]). This grouping of terms with different signs into the spin determinant is similar to "blocking" algorithms, e.g., [17], and it allows us to substantially weaken the fermion sign problem.

D. Path-integral Monte Carlo procedure for jellium

The above formulas have been applied successfully to multicomponent dense quantum plasma simulations [31,33,35,50], to the electron-hole plasmas in semiconductors [36,37], as well as to the quark-gluon plasma [38,39]. It is therefore desirable to retain the same program also for the simulation of jellium where the positive component (protons) is treated as a homogeneous static background. This has the advantage that both components are treated consistently. In particular, the background contribution will be automatically adjusted to the chosen particle number (which would not be the case if we used the known corrections for the case of an infinite system).

To perform the transition to the case of jellium with minimal changes, we set the potential energy contributions of the protons—the p-p and p-e interactions in the exponent of the high-temperature density matrices—to zero. Thus expression (27) is reduced to

$$U = \frac{1}{n+1}\sum_{l=0}^{n}U_e(X_e^{(l)},\Delta\beta). \qquad (29)$$

At the same time, the interaction terms Ψ_{ep} and Ψ_{pp} are retained as they produce the energy contribution of the "background." With this, the proton component is treated as an ideal gas of given density and temperature with the proton number always matching that of the electrons, guaranteeing charge neutrality. With these trivial changes, expressions (25), (26), and (29) are well suited for efficient fermionic PIMC simulations of jellium using standard METROPOLIS Monte Carlo techniques (see, e.g., [12,15,16]). In our Monte Carlo scheme, we use three different types of moves, where either electronic ($q_{t,e}$) or positive charge coordinate ($q_{p,h}$) or the individual electronic beads ($\eta_t^{(k)}$) are moved until convergence of the calculated values is reached.

Computer simulations of disordered systems, such as plasmas, require an accurate account of the long-range Coulomb forces since they strongly affect the thermodynamic and transport properties. Accurate simulations sometimes require up to a million particles in the main Monte Carlo cell. (While in PIMC simulations such numbers are not feasible, the large number of "time slices" gives rise to a comparable or even larger effective system size.) Thus, the larger the number of charged particles in the main cell, the more acute is the problem of an efficient evaluation of the Coulomb interaction contributions. To reduce boundary effects, periodic boundary conditions (PBCs) are usually imposed on the main Monte Carlo cell, and they have to be properly combined with the long-range Coulomb forces. One way to do this is the Ewald summation method; however, the usual procedure invokes an artificial nonisotropic electric "crystalline field" in the spatially uniform and isotropic Coulomb system. Moreover, periodicity artifacts are a heavy processor load in computer simulations. To avoid the "crystalline field," recently a modified Ewald scheme has been derived and applied to Coulomb systems [40]. This scheme uses suitable angle averages and is used below for particles interacting via the Kelbg potential. We expect that this extension is justified because the Kelbg and Coulomb potentials have identical long-range asymptotics.

To implement this concept, we identically rewrite the Kelbg potential as the sum of a short-range part, $\Delta\Phi_{ab}(x_{ab};\beta) = \Phi_{ab}(x_{ab};\beta) - \frac{e_a e_b}{\lambda_{ab} x_{ab}}$, and the long-range Coulomb potential,

$$\Phi_{ab}(x_{ab};\beta) = \Delta\Phi_{ab}(x_{ab};\beta) + \frac{e_a e_b}{\lambda_{ab} x_{ab}}. \tag{30}$$

Following Ref. [40], after averaging over all orientations of the main Monte Carlo cell, we obtain a potential $\tilde{\Phi}_{ab}(x_{ab};\beta)$ that accounts for PBC, for distances $x_{ab} < x_m$,

$$\begin{aligned}\tilde{\Phi}_{ab}(x_{ab};\beta) &= \Delta\Phi_{ab}(x_{ab};\beta) + \theta(x_m - x_{ab})\frac{e_a e_b}{\lambda_{ab} x_{ab}} \\ &\quad \times \left\{1 + \frac{1}{2}\left(\frac{x_{ab}}{x_m}\right)\left[\left(\frac{x_{ab}}{x_m}\right)^2 - 3\right]\right\} \\ &= \Phi_{ab}(x_{ab};\beta) + [\theta(x_m - x_{ab}) - 1]\,\frac{e_a e_b}{\lambda_{ab} x_{ab}} \\ &\quad + \frac{1}{2}\theta(x_m - x_{ab})\frac{e_a e_b}{\lambda_{ab} x_m}\left[\left(\frac{x_{ab}}{x_m}\right)^2 - 3\right],\end{aligned} \tag{31}$$

where $\theta(x_m - x_{ab})$ is the Heaviside step function. The parameter x_m, defined by $\frac{4}{3}\pi x_m^3 = L^3$, is the radius of the volume-equivalent sphere of the main Monte Carlo cell of length L. The effective pair potential $\tilde{\Phi}$, Eq. (31), has the following properties:

(i) At small distances, $x < x_m$, it tends to the Kelbg potential with PBC corrections arising from its long-range Coulomb asymptotic.

(ii) At large distances, $x > x_m$, due to the coincidence of the long-range asymptotics of the Kelbg and Coulomb potentials, the effective potential $\tilde{\Phi}$ tends to zero.

In expressions (25) and (29) and related calculations, we now replace the potential $\Phi_{ab}(x_{ab};\beta)$ with $\tilde{\Phi}_{ab}(x_{ab};\beta)$, thereby accounting for PBC effects. Note that one has to add to the first term in curly brackets in Eq. (25) a constant equal to $-\frac{3e_a e_b(N_e+N_p)}{16\pi\lambda_{ab}x_m}$ [40]. An analogous constant shift appears in the sum Eq. (29), but it is not important in the following, and it will therefore be omitted.

The main contribution to the path-integral representation of the partition function comes from configurations for which the typical size of the clouds of electronic beads is of the order of the thermal wavelength λ of the electrons. In the simulations below, we use up to about 100 electrons in the basic MC cell. Due to this limitation, we have a related restriction on the size of the MC cell for a given density.

Let us note another important improvement made in the present simulations. In our previous calculations, the determinants of the exchange matrices were only computed for particles belonging to the main Monte Carlo cell. However, for high degeneracy, $n\lambda^3 \gg 1$, the thermal wavelength (and the typical size of the electronic clouds of beads) may easily exceed the box size L. So beads of electrons belonging to the main cell can penetrate into neighboring images of the main cell, and vice versa. This requires a modified treatment of exchange in the PIMC simulations: it is necessary to include exchange effects between particles in the main MC cell and their images in the neighboring cells as well. Therefore, in the present calculations we take into account the exchange interactions of electrons with the electrons from the $(3^3 - 1)$ nearest-neighbor cells [51].

These are the main modifications to the PIMC algorithm, compared to our earlier work. Following the previous PIMC studies of the finite-temperature UEG, we separately study the polarized and unpolarized cases. This substantially simplifies the sums over the total electron spin s. Our simulations with the improved treatment of the electronic exchange are first tested for an ideal quantum system. The agreement with the known analytical results for an ideal finite-temperature Fermi gas is found to be very good, up to densities where the degeneracy parameter $n\lambda^3$ reaches values of the order of 100. This is demonstrated below in Figs. 2 and 3.

III. SIMULATION RESULTS

We now apply the theoretical scheme developed in the preceding sections to unpolarized and polarized jellium. Below, the density of the electrons is characterized by the Brückner parameter, $r_s = a/a_B$, defined as the ratio of the mean distance between particles, $a = [\frac{3}{4\pi n_e}]^{1/3}$, and the Bohr radius, a_B, where n_e is the electron density. Temperatures will be given in units of the Fermi energy, $\Theta = k_B T/E_F$.

We now present our fermionic path-integral Monte Carlo simulation results for the energy of the uniform electron gas, based on Eq. (25), with the simplifications discussed above. We use the same density and temperature interval that was studied in Ref. [24]: $r_s \geqslant 1$ and $\Theta = 0.0625, \ldots, 8$. Higher densities are not considered since there the sign problem is too severe and the data are not reliable.

For the present simulations, we varied both the particle number, in the range of $N_e = N_p = 50$–100, and the number of beads, in the range $M = 20$–90. Larger bead numbers are presently not feasible for such large systems. This interval of N and M has been used to perform an extrapolation to the macroscopic limit. Toward that end, we first performed an extrapolation $N \to \infty$ for fixed values of M. These extrapolated data were then used in a second extrapolation with respect to the bead number, $M \to \infty$. This procedure is demonstrated in Fig. 1 for the unpolarized case and the parameters $\Theta = 0.625$ and $r_s = 1$. We purposely selected the most difficult case in which the accessible number of beads is, most likely, insufficient to produce a reliable macroscopic result giving rise to a large statistical error. However, for

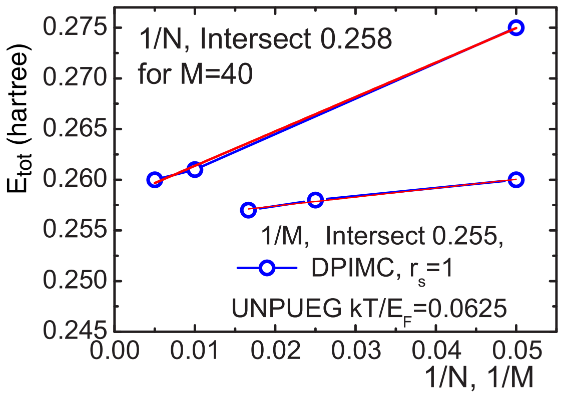

FIG. 1. (Color online) Illustration of the extrapolation of the total energy with respect to the number of beads M and the particle number N. First, for a fixed value of M, an extrapolation $N \to \infty$ is performed (upper curve). Subsequently, these results are extrapolated with respect to M (lower curve). Results are for the unpolarized case with $\Theta = 0.0625$ and $r_s = 1$. DPIMC data points are in blue, while the extrapolation (fit) is shown by the red line.

all other situations, the extrapolation works satisfactorily and produces a statistical error not exceeding a few percent.

Figures 2 and 3 show the results for a polarized electron gas and for the unpolarized case, respectively. The left columns show the total energy for four different temperatures, whereas the right columns contain the correlation energy, which was calculated as $E_c = E_{\text{tot}} - E_0 - E_{x,\text{HF}}$, subtracting from the total energy the kinetic energy and the finite-temperature Hartree-Fock (mean field plus exchange) energy of Ref. [24]. Since E_{tot} and $E_0 + E_{x,\text{HF}}$ are of the same order of magnitude, the remainder (the correlation energy) is very susceptible to different approximations and allows for sensitive comparisons of our results to those of Ref. [24].

A. Polarized electron gas

Consider first the polarized case, Fig. 2. The much improved treatment of fermionic exchange (see above) is confirmed by the four plots for the total energy (left columns). The curve denoted "E_0" shows the (kinetic) energy of an ideal polarized Fermi gas at finite temperature computed from the relevant Fermi integral. The curves "DPIMC E_0" show the same result obtained with our fermionic PIMC simulations (in these simulations, all interaction terms were turned off). For the two highest temperatures, $\Theta = 8$ and 1, the results coincide practically for all densities. For $\Theta = 0.25$, small deviations are seen at the highest density, $r_s = 1$, whereas for $\Theta = 0.0625$, deviations are visible up to $r_s \sim 3$. This behavior is a very good test for the order of magnitude of the error and for the reliability of our simulations.

If interactions are included, the total energy is lower compared to the ideal case. The curves are denoted by "DPIMC" and are compared to the corresponding restricted PIMC data of Brown *et al.* [24] labeled "RPIMC." Again, the agreement over the entire temperature interval is rather good. An exception is the point $r_s = 1$ corresponding to the highest density. For $\Theta = 0.25$, our data are substantially lower than RPIMC. Interestingly, for $\Theta = 0.0625$ the agreement is significantly better, although the accuracy of our results is most likely lower due to the increased sign problem. Also, notice the fermionic ("signful") PIMC simulations of Ref. [24] labeled "SFPIMC" that are plotted with the open (pink) circles. For low densities, we observe good agreement with our data, whereas for $r_s \lesssim 4$ there are significant deviations. At these points, the SFPIMC data already carry large error bars, and we expect that our results, due to the various improvements of the simulation approach, are more accurate.

In contrast to the rather good agreement of the total energies, there is a quite large deviation between DPIMC and RPIMC for the correlation energy. For different densities, the deviations can be positive or negative: for high temperatures ($\Theta \geqslant 1$), our values are generally higher, whereas for $\Theta = 0.25, 0.0625$ our results are substantially lower, at high densities $r_s \leqslant 4$.

Possible reasons for these deviations are (a) quantum effects in the interaction of electrons with the uniform background described, in our calculations, by the effective Kelbg pseudopotential, instead of the Coulomb potential. The Kelbg pseudopotential is defined by the logarithm of the high-temperature asymptotic of the quantum two-particle density matrix. The Coulomb potential cannot be obtained in the same way as the classical density matrix of two oppositely charged particles diverges at small interparticle distances. Other sources for deviations are (b) the different particle numbers used in DPIMC and RPIMC, and (c) finite-size correction that are applied to the RPIMC data [24] but not to our results—we instead performed an extrapolation to the macroscopic limit; cf. Fig. 1.

B. Unpolarized electron gas

Consider now the energies in the case of an unpolarized electron gas; see Fig. 3. Again, the ideal system constitutes a benchmark for the treatment of fermionic exchange in our simulations. Here the agreement with the analytical results is slightly worse than in the polarized case before, due to poorer convergence. Deviations are seen already for $\Theta = 1$ and $r_s = 1$ and continue to grow for $\Theta = 0.25$ and 0.0625. The comparison of the results for the interacting electron gas with the RPIMC data of Ref. [24] is similar to that in the polarized case. At temperatures $\Theta \gtrsim 1$, the agreement is very good. Deviations start to appear for $\Theta = 1$ at $r_s = 1$. At the lowest temperature, $\Theta = 0.0625$, deviations are observed for all densities. Comparing again with the fermionic (SFPIMC) data of Ref. [24], cf. the data point at $\Theta = r_s = 1$, we observe dramatic deviations because the SFPIMC results of Ref. [24] carry a very large error. Interestingly, in our case the error appears to be much smaller, which we attribute to the improved treatment of fermionic exchange (taking into account exchange contributions from electron images in the nearest-neighbor cells) and the use of the exchange determinant, which constitutes an efficient approach to grouping different exchange contributions together that partially compensate each other and increase the sign in the simulations. The difference in the correlation energies of our results compared to Ref. [24] are larger than in the polarized case, and the discrepancies now extend to $r_s = 10$. A possible reason for the increased deviations in the unpolarized case is the use of twice as many particles ($N = 66$) in Ref. [24]. In contrast, in our DPIMC simulations, doubling the particle number was not feasible.

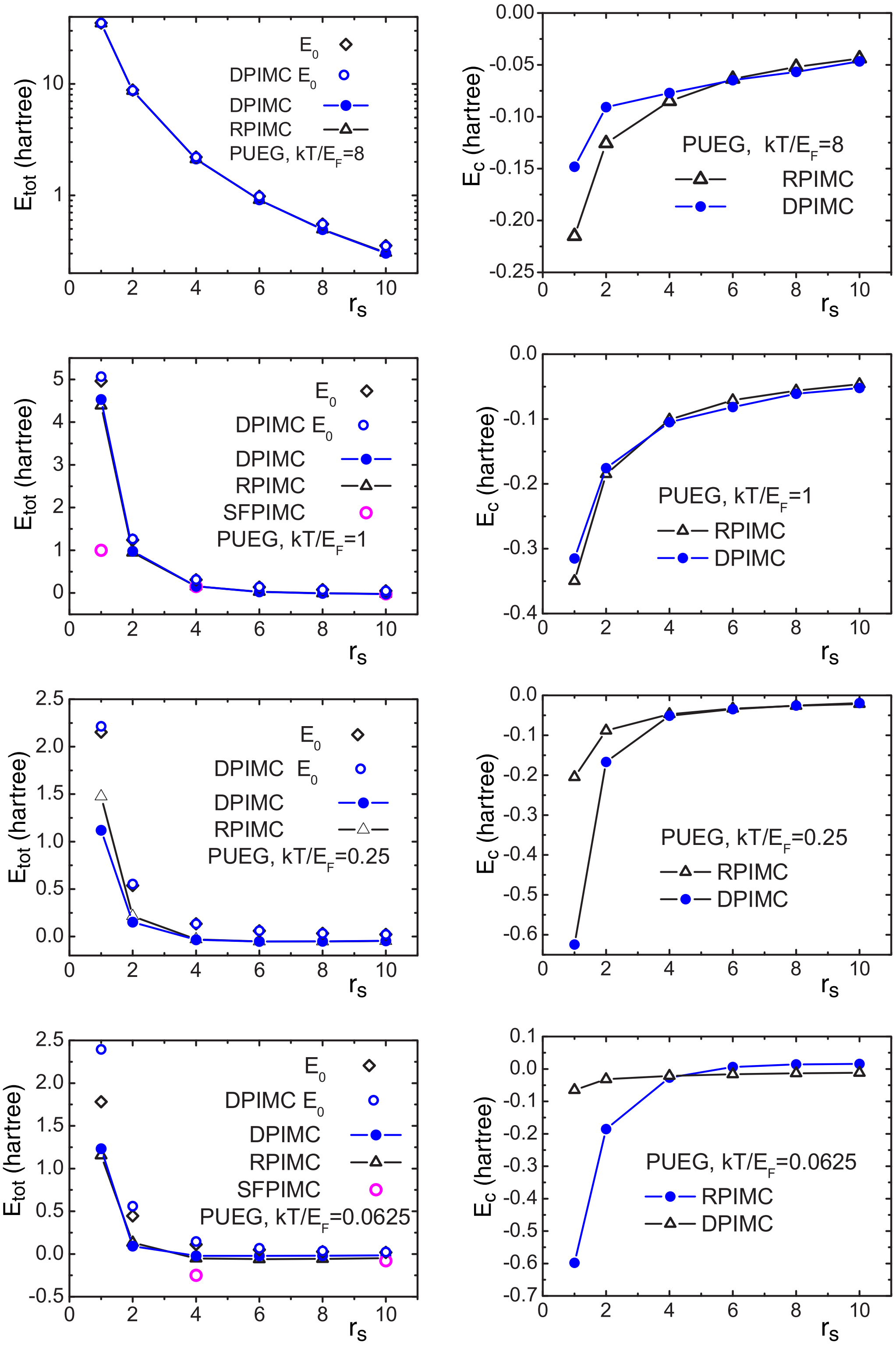

FIG. 2. (Color online) Total energy per particle (left column) and correlation energy per particle (right column) for a polarized ideal (E_0) and interacting electron gas (PUEG) with temperatures ranging from $\Theta = 8$ to 0.0625; see text in the graphs. Comparison of restricted PIMC (RPIMC, Ref. [24]), fermionic PIMC (SFPIMC, open pink circles [24]), and the present DPIMC results. The correlation energy is given by $E_c = E_{\text{tot}} - E_0 - E_{x,\text{HF}}$ using the Hartree-Fock energy of Ref. [24]; see the main text.)

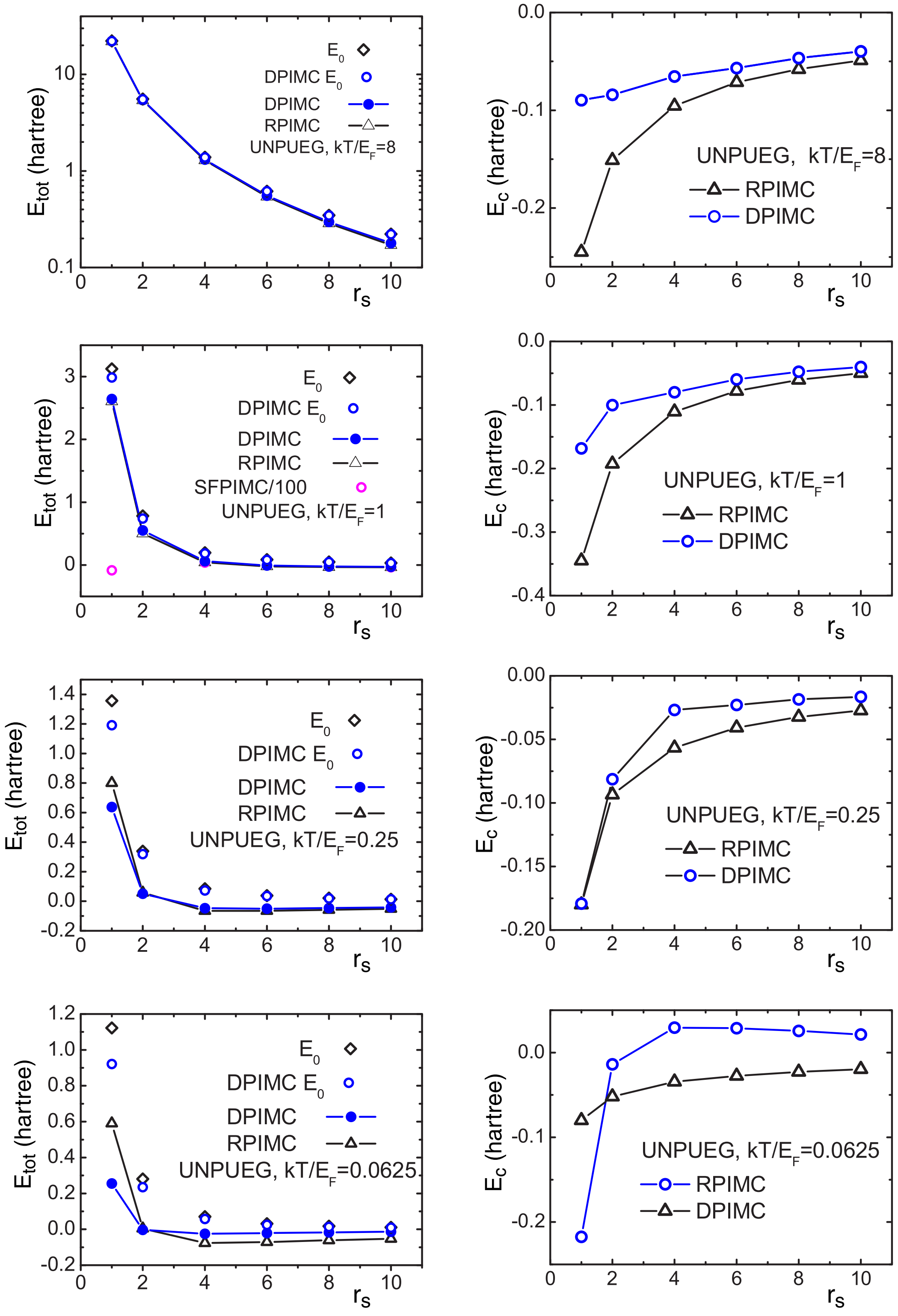

FIG. 3. (Color online) Same as Fig. 2 but for an unpolarized electron gas.

IV. DISCUSSION

In this paper, we have presented improved direct fermionic path-integral Monte Carlo (DPIMC) simulations for the thermodynamic properties of the uniform electron gas over a wide density and temperature range relevant for warm dense matter conditions. The results were produced with a previously developed code for two-component Coulomb systems; herein, for the treatment of the homogeneous background, the spatial correlations of the particles of the second component were neglected. The present simulations contain two main improvements: first, we included long-range Coulomb effects via Ewald summation, where an angle average was performed, as proposed by Yakub *et al.* [40]. Second, we improved the treatment of fermionic exchange in the case of strongly degenerate electrons. For cases in which the electron thermal wavelength exceeds the length of the simulation cell, we included not only exchanges between particles in the main Monte Carlo cell, but also with electrons from the nearest-neighbor cells. This had a drastic effect on the computed energy, and good accuracy was demonstrated for the limiting case of an ideal Fermi gas, which matches the analytically known results very well. We observed deviations for the lowest temperatures ($\Theta = 0.0625,1$) and highest densities, $r_s = 1$. Evidently, here it would be desirable to include also exchanges with electron images from the next-to-nearest-neighbor cells. These simulations require an order of magnitude more CPU time and are presently not feasible.

For the interacting case, we compared our direct fermionic PIMC simulations with recent restricted PIMC simulations and direct (signful) simulations by Brown *et al.* [24]. First we notice that our simulations carry a much smaller statistical error than the signful results of Ref. [24], and they are significantly closer to the RPIMC data at high degeneracy. This is attributed to the improved treatment of exchange in our approach. Second, the comparison to the RPIMC results revealed very good agreement for all densities, $r_s \gtrsim 1$, for temperatures above the Fermi energy. For lower temperatures, we observe good agreement for moderate densities, $r_s \gtrsim 4$, for the spin-polarized case, and slightly larger deviations for the unpolarized electron gas. The good agreement, over such a broad range of parameters, between the two independent approaches that involve entirely different approximations is certainly remarkable, and we consider it to be our main result. Thus, we have mapped out the parameter range where the predictions for the energy of the UEG can be considered reliable.

Furthermore, an analysis of the deviations between our DPIMC results and the RPIMC data of Ref. [24] will allow us to develop strategies for improved simulations in the future. While RPIMC is presently not able to correctly treat the kinetic energy at high degeneracy, our DPIMC simulations have achieved an improved treatment that should make accurate simulations for $r_s \sim 1.5$ possible in the near future, at the cost of a substantial increase in CPU time. On the other hand, while the total energies of our DPIMC simulations are in overall good agreement with the RPIMC results of Ref. [24], we observe significant deviations of the correlation energies, particularly in the unpolarized case. Possible reasons are (a) the different treatment of quantum effects in the interaction of electrons with the uniform background, (b) the different number of particles in the two simulations, and (c) finite-size corrections that are applied in Ref. [24] but not in our results. Here more analysis has to be done to arrive at a one-to-one comparison.

A useful first step could be a detailed comparison for a given, possibly small, particle number without any finite-size corrections. Here, for the model case $N = 4$, recently accurate energy data for the entire density range have been presented [52]. This paper uses the recently developed configuration path-integral Monte Carlo (CPIMC) approach [53]; for an introduction to the method, see Ref. [54]. This method allows for *ab initio* simulations in the opposite parameter range $r_s \lesssim 1$ [55]. Another novel approximate treatment of fermionic exchange cycles was recently proposed [56]. A combination of these concepts with the DPIMC approach of the present work and RPIMC should allow one to achieve reliable theoretical predictions for the uniform electron gas in the entire parameter range in the near future.

ACKNOWLEDGMENTS

We acknowledge stimulating discussions with T. Schoof, S. Groth, and T. Dornheim (Kiel) and J.W. Dufty and V. Karasiev (University of Florida). This work has been supported by the Russian Science Foundation via Grant No. 14-50-00124 and Deutsche Forschungsgemeinschaft via SFB TR-24. Computations were performed at the "Fermion" compute-cluster of the Institute for Theoretical Physics and Astrophysics of Kiel University and at the North-German Supercomputing Center (HLRN) via Grant No. SHP006.

[1] M. D. Knudson, M. P. Desjarlais, R. W. Lemke, T. R. Mattsson, M. French, N. Nettelmann, and R. Redmer, Probing the interiors of the ice giants: Shock compression of water to 700 GPa and 3.8 g/cm^3, Phys. Rev. Lett. **108**, 091102 (2012).

[2] J. D. Lindl *et al.*, The physics basis for ignition using indirect-drive targets on the National Ignition Facility, Phys. Plasmas **11**, 339 (2004).

[3] L. B. Fletcher *et al.*, Observations of continuum depression in warm dense matter with x-ray Thomson scattering, Phys. Rev. Lett. **112**, 145004 (2014).

[4] W. D. Kraeft, D. Kremp, W. Ebeling, and G. Röpke, *Quantum Statistics of Charged Particle Systems* (Akademie-Verlag, Berlin, 1986).

[5] *Kinetic Theory of Nonideal Plasmas*, edited by M. Bonitz and W. D. Kraeft [J. Phys.: Conf. Ser. **11** (2005)].

[6] B. Holst, R. Redmer, and M. P. Desjarlais, Thermophysical properties of warm dense hydrogen using quantum molecular dynamics simulations, Phys. Rev. B **77**, 184201 (2008).

[7] F. Lambert, J. Clerouin, and G. Zerah, Very-hightemperature molecular dynamics, Phys. Rev. E **73**, 016403 (2006).

[8] D. M. Ceperley and B. J. Alder, Ground state of the electron gas by a stochastic method, Phys. Rev. Lett. **45**, 566 (1980).

[9] J. J. Shepherd, G. Booth, A. Grüneis, and A. Alavi, Full configuration interaction perspective on the homogeneous electron gas, Phys. Rev. B **85**, 081103(R) (2012).

[10] J. J. Shepherd, G. Booth, and A. Alavi, Investigation of the full configuration interaction quantum Monte Carlo method using homogeneous electron gas models, J. Chem. Phys. **136**, 244101 (2012).

[11] R. P. Feynman and A. R. Hibbs, *Quantum Mechanics and Path Integrals* (McGraw-Hill, New York, 1965).

[12] *The Monte Carlo and Molecular Dynamics of Condensed Matter Systems*, edited by K. Binder and G. Cicotti (SIF, Bologna, 1996).

[13] D. M. Ceperley, in Ref. [12], pp. 447–482.

[14] D. M. Ceperley, Path integrals in the theory of condensed helium, Rev. Mod. Phys. **67**, 279 (1995).

[15] V. M. Zamalin, G. E. Norman, and V. S. Filinov, *The Monte Carlo Method in Statistical Thermodynamics* (Nauka, Moscow, 1977) (in Russian).

[16] *Introduction to Computational Methods for Many Body Systems*, edited by M. Bonitz and D. Semkat (Rinton, Princeton, NJ, 2006).

[17] R. Egger, W. Häusler, C. H. Mak, and H. Grabert, Crossover from Fermi liquid to Wigner molecule behavior in quantum dots, Phys. Rev. Lett. **82**, 3320 (1999).

[18] A. V. Filinov, M. Bonitz, and Yu. E. Lozovik, Wigner crystallization in mesoscopic 2d electron systems, Phys. Rev. Lett. **86**, 3851 (2001).

[19] B. Militzer and E. L. Pollock, Variational density matrix method for warm, condensed matter: Application to dense hydrogen, Phys. Rev. E **61**, 3470 (2000).

[20] B. Militzer, First principles calculations of shock compressed fluid helium, Phys. Rev. Lett. **97**, 175501 (2006).

[21] V. S. Filinov, M. Bonitz, and V. E. Fortov, High-density phenomena in hydrogen plasma, JETP Lett. **72**, 245 (2000).

[22] V. S. Filinov, V. E. Fortov, M. Bonitz, and P. R. Levashov, Phase Transition in strongly degenerate hydrogen plasma, JETP Lett. **74**, 384 (2001) [Pis'ma Zh. Eksp. Teor. Fiz. **74**, 422 (2001)].

[23] M. Bonitz *et al.*, Theory and simulation of strong correlations in quantum Coulomb systems, J. Phys. A **36**, 5921 (2003).

[24] E. W. Brown, B. K. Clark, J. L. DuBois, and D. M. Ceperley, Path-integral Monte Carlo simulation of the warm dense homogeneous electron gas, Phys. Rev. Lett. **110**, 146405 (2013).

[25] V. V. Karasiev, T. Sjostrom, J. Dufty, and S. B. Trickey, Accurate homogeneous electron gas exchange-correlation free energy for local spin-density calculations, Phys. Rev. Lett. **112**, 076403 (2014).

[26] B. Militzer, Ph.D. dissertation, University of Illinois at Urbana-Champaign, 2000.

[27] V. S. Filinov, Phase transition in strongly degenerate hydrogen plasma, J. Phys. A **34**, 1665 (2001).

[28] V. S. Filinov, Analytical contradictions of the fixed-node density matrix, High Temp. **52**, 615 (2014).

[29] E. W. Brown, J. L. DuBois, M. Holzmann, and D. M. Ceperley, Exchange-correlation energy for the three-dimensional homogeneous electron gas at arbitrary temperature, Phys. Rev. B **88**, 081102(R) (2013).

[30] E. W. Brown, J. L. DuBois, M. Holzmann, and D. M. Ceperley, Erratum: Exchange-correlation energy for the three-dimensional homogeneous electron gas at arbitrary temperature [Phys. Rev. B **88**, 081102(R) (2013)], Phys. Rev. B **88**, 199901(E) (2013).

[31] M. Bonitz, V. S. Filinov, V. E. Fortov, P. R. Levashov, and H. Fehske, Crystallization in two-component coulomb systems, Phys. Rev. Lett. **95**, 235006 (2005).

[32] V. S. Filinov, V. E. Fortov, M. Bonitz, and D. Kremp, Pair distribution functions of dense partially ionized hydrogen, Phys. Lett. A **274**, 228 (2000).

[33] V. S. Filinov, M. Bonitz, W. Ebeling, and V. E. Fortov, Thermodynamics of hot dense H-plasmas: Path integral Monte Carlo simulations and analytical approximations, Plasma Phys. Control. Fusion **43**, 743 (2001).

[34] V. S. Filinov, P. Levashov, M. Bonitz, and V. E. Fortov, Thermodynamics of hydrogen and hydrogen-helium plasma mixtures, Contrib. Plasma Phys. **45**, 258 (2005).

[35] P. R. Levashov, V. Filinov, M. Bonitz, and V. E. Fortov, Path integral Monte Carlo calculations of helium and hydrogen-helium plasma thermodynamics and deuterium shock Hugoniot, J. Phys. A **39**, 4447 (2006).

[36] V. Filinov, M. Bonitz, P. Levashov, V. Fortov, W. Ebeling, and M. Schlanges, Plasma phase transition in hydrogen and electron-hole plasmas, Contrib. Plasma Phys. **43**, 290 (2003).

[37] V. S. Filinov, M. Bonitz, P. R. Levashov, V. E. Fortov, W. Ebeling, M. Schlanges, and S. W. Koch, Plasma phase transition in dense hydrogen and electron-hole plasmas, J. Phys. A **36**, 6069 (2003).

[38] V. S. Filinov, M. Bonitz, Y. B. Ivanov, P. R. Levashov, and V. E. Fortov, Quantum Monte Carlo simulations of strongly coupled quark-gluon plasma, Contrib. Plasma Phys. **52**, 135 (2012).

[39] V. S. Filinov, Yu. B. Ivanov, V. E. Fortov, M. Bonitz, and P. R. Levashov, Color path-integral Monte Carlo simulations of quark-gluon plasma: Thermodynamic and transport properties, Phys. Rev. C **87**, 035207 (2013).

[40] E. Yakub and C. Ronchi, A new method for computation of long ranged coulomb forces in computer simulation of disordered systems, J. Low Temp. Phys. **139**, 633 (2005).

[41] G. D. Mahan, *Many-Particle Physics* (Plenum, New York, 2000).

[42] G. Kelbg, Theorie des Quanten-Plasmas, Ann. Phys. (Leipzig) **12**, 219 (1963).

[43] W. Ebeling, H. J. Hoffmann, and G. Kelbg, Quantenstatistik des Hochtemperatur-Plasmas im thermodynamischen Gleichgewicht, Contrib. Plasma Phys. **7**, 233 (1967), and references therein.

[44] A. Filinov, M. Bonitz, and W. Ebeling, Improved Kelbg potential for correlated Coulomb systems, J. Phys. A **36**, 5957 (2003).

[45] A. V. Filinov, V. O. Golubnychiy, M. Bonitz, W. Ebeling, and J. W. Dufty, Temperature-dependent quantum pair potentials and their application to dense partially ionized hydrogen plasmas, Phys. Rev. E **70**, 046411 (2004).

[46] W. Ebeling, A. Filinov, M. Bonitz, V. Filinov, and T. Pohl, The method of effective potentials in the quantum-statistical theory of plasmas, J. Phys. A **39**, 4309 (2006).

[47] C. Deutsch, Nodal expansion in a real matter plasma, Phys. Lett. A **60**, 317 (1977).

[48] D. Klakow, C. Toepffer, and P.-G. Reinhard, Hydrogen under extreme conditions, Phys. Lett. A **192**, 55 (1994).

[49] V. S. Filinov, Pseudopotential model of nonideal degenerate plasma, High Temp. **13**, 1065 (1975); Influence of plasma nonideality on electron degeneration, **14**, 225 (1976).

[50] V. S. Filinov, M. Bonitz, V. E. Fortov, W. Ebeling, H. Fehske, D. Kremp, W. D. Kraeft, V. Bezkrovny, and P. Levashov, Monte Carlo simulations of dense quantum plasmas, J. Phys. A **39**, 4421 (2006).

[51] As a second step, this could be extended to the $(5^3 - 1)$ nearest- and next-nearest-neighbor cells, until convergence is reached. Due to the rapidly increasing computational effort, this has not been possible in the present work, and it will be studied in a forthcoming work.

[52] T. Schoof, S. Groth, and M. Bonitz, Towards ab initio thermodynamics of the electron gas at strong degeneracy, Contrib. Plasma Phys. **55**, 136 (2015).

[53] T. Schoof, M. Bonitz, A. Filinov, D. Hochstuhl, and J. W. Dufty, Configuration path integral Monte Carlo, Contrib. Plasma Phys. **51**, 687 (2011).

[54] S. Groth, T. Schoof, and M. Bonitz, *Complex Plasmas: Scientific Challenges and Technological Opportunities*, edited by M. Bonitz, K. Becker, J. Lopez, and H. Thomsen (Springer, Berlin, 2014).

[55] T. Schoof, S. Groth, J. Vorberger, and M. Bonitz, Ab initio thermodynamic results for the degenerate electron gas at finite temperature, arXiv:1502.04616.

[56] J. L. DuBois, B. J. Alder, and E. W. Brown, Overcoming the fermion sign problem in homogeneous systems, arXiv:1409.3262.